

# MAXIMUM PERFORMANCE OF CAVITIES AFFECTED BY THE HIGH-FIELD Q-SLOPE\*

G. Ciovati<sup>†</sup>, Jefferson Lab, Newport News, VA, USA  
I. Parajuli, A. Gurevich, Old Dominion University, Norfolk, VA, USA

## Abstract

The performance of high-purity, bulk niobium SRF cavities treated by chemical processes such as BCP or EP is limited by the so-called high-field Q-slope (HFQS). Several models and experimental studies have been proposed and performed over the years to understand the origin of these anomalous losses but a consensus on what these origins are is yet to be established. In this contribution, we present the results of the RF tests of several 1.3 GHz single-cell cavities limited by the HFQS and tested using a variable input coupler. This allowed us to maintain close to critical coupling even at high field. The data showed that the HFQS did not saturate with the rf field and that in some cases a RF power of up to 200 W at 2 K could be sustained without quench.

## INTRODUCTION

The performance of superconducting radio-frequency (SRF) bulk Nb cavities treated by buffered chemical polishing (BCP) or electropolishing (EP) is limited at high accelerating gradients by the so-called “high-field Q-slope” (HFSQ) or “Q-drop”. This phenomenon is characterized by a nearly exponential decrease of the quality factor,  $Q_0$ , with increasing peak surface magnetic field,  $B_p$ , above ~90 mT at or below a temperature of 2 K [1]. An empirical method to recover the quality factor at high fields is to bake the cavities at ~120 °C for 24-48 h [1].

Many models have been proposed in the literature to explain the origin of the HFQS, including roughness of the surface, penetration of vortices along grain boundaries, RF current pairbreaking, reduced critical field due to surface contamination and tunnelling through a defective oxide. However, results of experiments seem to contradict some of the predictions of those models so that there is no consensus on the origin of the HFQS [1].

One of the model attributes the HFQS to the presence of normal-conducting nano-hydrides that are superconducting by proximity at low field, but become normal-conducting above a threshold breakdown field [2]. The model assumes a normal distribution for the thickness of the hydrides, which results in a distribution of breakdown fields. The model predicts that at sufficiently high fields the surface resistance should saturate with the RF field, once all hydrides precipitates become normal-conducting.

\* Authored by Jefferson Science Associates, LLC under U.S. DOE Contract No. DE-AC05-06OR23177. The work of I. P. and A. G. is supported by NSF Grant PHY 100614-010.

<sup>†</sup> gciovati@jlab.org

We attempted to test some of the models of HFQS by performing the cryogenic high-power RF tests of six 1.3 GHz single-cell cavities, all limited by the high-field Q-slope, using a variable input coupler to allow coupling of greater than 90% of the forward power into the cavity.

## CAVITY TEST RESULTS

The single-cell 1.3 GHz cavities used for this study were made from high-purity (residual resistivity ratio greater than 300) ~3 mm thick Nb. Two of them, labelled N3 and PJ1-1 were made from large-grain Nb disks from OTIC Ningxia, China, the other ones, labelled RTD-TD01, EZ-SSC-01, TE1G001 and TE1NS001, were made of standard fine-grain Nb from Tokyo-Denkai, Japan. The final treatment of N3 and PJ-1 was BCP, whereas it was EP for the other cavities.

N3 and PJ1-1 have the TESLA/XFEL center-cell shape ( $G = 269.8 \Omega$ ,  $B_p/E_{acc} = 4.12 \text{ mT}/(\text{MV}/\text{m})$ ), whereas the other cavities have the TESLA/XFEL end-cell shape ( $G = 277.8 \Omega$ ,  $B_p/E_{acc} = 4.23 \text{ mT}/(\text{MV}/\text{m})$ ) [3]. The final preparation prior to the RF test of each cavity consisted of high-pressure rinse with ultra-pure water, assembly of the pickup antenna and of the variable input coupler [4], evacuation and leak check. For each test, the cavity is inserted in a vertical cryostat with a residual magnetic field of ~2 mG and cooled with liquid helium to 2 K, with a typical temperature gradient of ~0.4 K/cm along the cell. Figure 1 shows a picture of the cavity assembled on a vertical test stand, prior to insertion in the cryostat.



Figure 1: Single-cell cavity N3 attached to a vertical test stand with a variable input coupler.

Table 1: Summary of the RF Performance at 2 K of the Six 1.3 GHz Single-Cell Cavities Used for This Study

Cavity Label	Nb Material	Treatment	$B_{p,max}$ (mT)	$Q_0$ at $B_{p,max}$	$P_{loss}$ at $B_{p,max}$ (W)	Limit
EZ-SSC-01	Fine-grain	EP	$153 \pm 8$	$(8.0 \pm 1.0) \times 10^8$	$200 \pm 10$	RF power
RDT-TD01	Fine-grain	EP	$161 \pm 8$	$(1.2 \pm 0.1) \times 10^9$	$153 \pm 16$	RF power
N3	Large-grain	BCP	$142 \pm 7$	$(7.0 \pm 0.5) \times 10^8$	$181 \pm 16$	Quench
PJ1-1	Large-grain	BCP	$141 \pm 7$	$(7.5 \pm 0.6) \times 10^8$	$180 \pm 14$	RF power
TE1G001	Fine-grain	EP	$117 \pm 6$	$(1.1 \pm 0.1) \times 10^{10}$	$8.7 \pm 0.7$	Quench
TE1NS001	Fine-grain	EP	$131 \pm 6$	$(1.2 \pm 0.1) \times 10^{10}$	$10.2 \pm 0.8$	Quench

The measured cavity performance parameters are listed in Table 1 and a summary plot of  $Q_0(B_p)$  at 2 K is shown in Fig. 2. For cavities TE1G001, TE1NS001 and N3, the breakdown fields were limited by a quench, whereas the other cavities were limited by the output power of the RF amplifier, ~350 W. No X-rays were detected in any of the tests, except for cavity EZ-SSC-01, for which a maximum dose rate of 4 mR/h with an onset of 152 mT, close to the maximum field.

The power dissipated in the cavity,  $P_{loss}$ , at the highest field was 150 W, 180 W and 200 W in cavities RDT-TD01, PJ1-1 and EZ-SSC-01, respectively. The power  $P_{loss}$  exceeding ~170 W was greater than the capacity of the pump used to maintain the temperature of the helium bath at 2.0 K (23.5 Torr), in which case the He bath temperature increased to ~2.04 K at the highest field in cavities PJ1-1 and EZ-SSC-01. The ratio of reflected power divided by the forward power at the maximum gradient was 25%, 1% and 0.3% for cavities RDT-TD01, PJ1-1 and EZ-SSC-01, respectively. The input antenna was too short and did not allow for a better coupling factor for RDT-TD01 at the highest field.

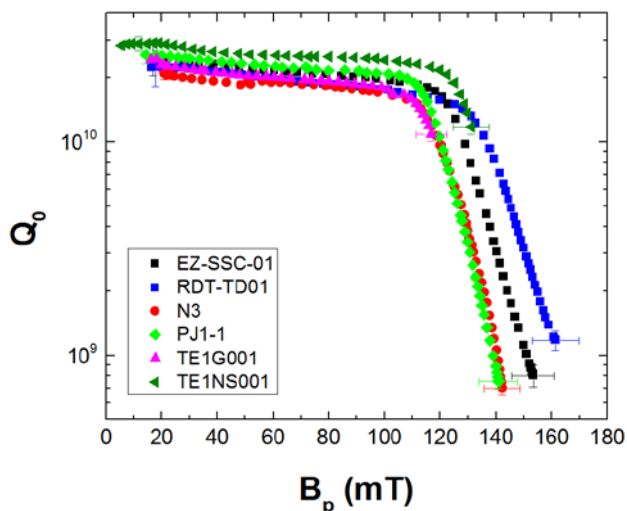


Figure 2: Summary of  $Q_0(B_p)$  measured at 2 K in six 1.3 GHz single-cell bulk Nb cavities. TE1G001, TE1NS001 and N3 were limited by quench, EZ-SSC-01, RDT-TD01 and PJ1-1 were limited by the available RF power.

The cavity RDT-TD01 was re-assembled on a different test stand and a temperature mapping system [5] was attached, besides the variable input coupler. After the standard cool-down, the temperature rise  $\Delta T$  at the outer cavity surface immersed in liquid helium at 2.0 K, was measured while increasing the rf field. The cavity was limited by quench and the last stable point was at 165 mT with a  $Q_0$  of  $2.8 \times 10^9$ . The temperature map at the highest stable point of operation is shown in Fig. 3. The cavity quenched at sensor No. 8 at  $140^\circ$ , where one of the major hotspots is located.

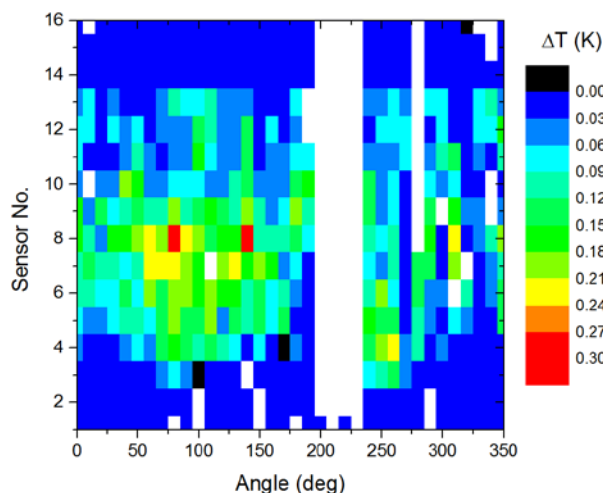


Figure 3: Unfolded temperature map at  $B_p = 165$  mT,  $P_{loss} = 68$  W for cavity RDT-TD01 at 2.0 K. Sensor 1 is at the top iris, sensor 16 is at the bottom beam tube, close to the iris. Sensor 8 is on the equator weld. Malfunctioning channels/sensors are shown in white in the color map.

## MODEL COMPARISON

The hydride model for the Q-drop predicts the field dependence of the surface resistance to be given by the following equation [2]:

$$R_s(B_p) = R_0 + \frac{\alpha_s R_n}{2} \left[ 1 - \operatorname{erf} \left( \frac{\frac{1}{B_p} - \frac{1}{B_0}}{\sqrt{2}\sigma} \right) \right] \quad (1)$$

where  $R_n$  and  $\alpha_s$  are the surface resistance and the surface density of the normal-conducting hydrides,  $B_0$  and  $\sigma$  are the mean and the width of the distribution of the hydrides

breakdown field, respectively.  $R_0$  is the surface resistance at fields lower than the onset of Q-drop.

Figure 4 shows the average surface resistance  $\langle R_s \rangle = G/Q_0$ , where  $G$  is the cavity geometry factor, as a function of  $B_p$  above 90 mT for the four cavities which were not affected by a premature quench. The solid lines in Fig. 4 were obtained from a non-linear fit of Eq. (1) using the Levenberg-Marquardt algorithm provided in Origin®. The values of the four fit parameters are listed in Table 2. The chi-square convergence tolerance had to be set to  $10^{-3}$  for the fit to converge. The parameters  $\alpha_s R_n$  and  $H_0$  are strongly correlated, resulting in a large uncertainty of the fit parameter values, as shown in Table 2.

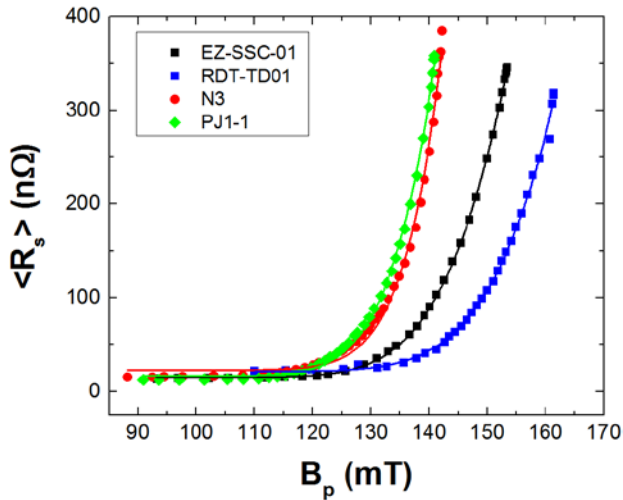


Figure 4: Average cavity surface resistance at 2.0 K as a function of  $B_p$  above 90 mT. Solid lines are fits to Eq. (1).

Table 2: Values of the Fit Parameters From the Non-Linear Fit of Eq. (1) to the Experimental  $R_s(B_p)$ -Data at High Field

Cavity Label	$R_0$ (nΩ)	$\alpha_s R_n$ (nΩ)	$B_0$ (mT)	$\sigma$ (1/mT)
EZ-SSC-01	$15 \pm 1$	$(17 \pm 8) \times 10^3$	$239 \pm 20$	$0.0011 \pm 1 \times 10^{-4}$
RDT-TD01	$21 \pm 2$	$(4 \pm 20) \times 10^4$	$296 \pm 174$	$0.0012 \pm 1 \times 10^{-4}$
N3	$23 \pm 2$	$(5 \pm 60) \times 10^6$	$488 \pm 1560$	$0.0013 \pm 1 \times 10^{-4}$
PJ1-1	$17 \pm 1$	$(7 \pm 14) \times 10^4$	$238 \pm 80$	$0.0011 \pm 2 \times 10^{-4}$

## HOT-SPOT DISSIPATION

The field dependence of the temperature rise on the outer surface at some hotspot locations is shown in Fig. 5. It changes from a power law  $\Delta T \propto B_p^n$  with  $n \sim 2$  between 60 mT and 130 mT to an exponential increase above  $\sim 140$  mT.

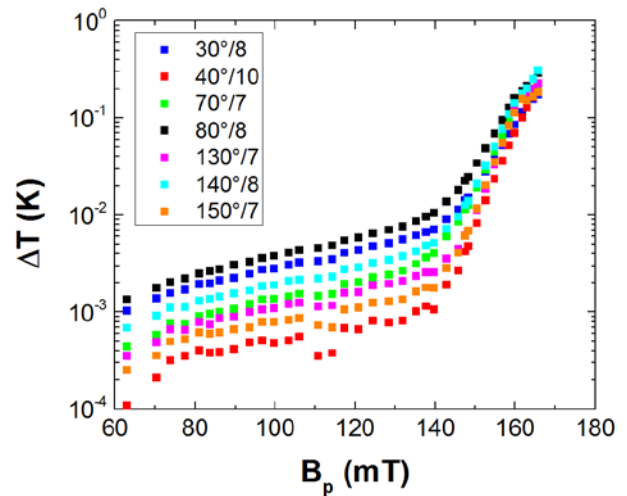


Figure 5: Temperature rise measured on the outer surface of cavity RDT-TD01 at 2 K at selected hotspots, identified by the angle/sensor No., as a function of  $B_p$ .

The temperature profile at  $130^\circ$  shows only one major hotspot at sensor 7. The temperature rise on the inner and outer surfaces due to an isolated source of additional losses at the inner surface, of size much smaller than the wall thickness, were calculated in [6]. Examples of such local power sources can be either non-superconducting precipitates or a bundle of trapped vortices. Figure 6 shows the temperature profile along the cavity meridian at  $130^\circ$ ,  $s$ , centred at the location of sensor 7, for different  $B_p$ -values. The solid lines are least-squares non-linear fits with Eq. (38) of Ref. [6]. Here  $\Delta T(r)$  depends on the following parameters:  $\beta = \kappa/d\alpha_K$ , where  $d$  is the wall thickness,  $\kappa$  is the thermal conductivity and  $\alpha_K$  is the Kapitza conductance, the additional power of the localized heat source  $P_0$  and  $\gamma = \frac{H_p^2}{2\alpha_K} \left[ \frac{\partial R_s}{\partial T} \right]_{T_m}$ . A value of  $\beta = 1.2$ , obtained for  $d = 2.8$  mm,  $\kappa = 10$  W/(m K) and  $\alpha_K = 3$  kW/(m<sup>2</sup> K), was used in these fits, except for the three highest  $B_p$ -values, for which  $\Delta T_{\max} > 2.17$  K. In the latter cases  $\beta$  was increased to 1.4, 1.6 and 2.4, reflecting a lower average  $\alpha_K$  over the hotspot area where the central part is overheated above the superfluid transition temperature. There is an asymmetry in some of the temperature profiles, moving from the top side of the cavity (negative  $s$ -values) to the bottom side with increasing field. The asymmetry may result from a partial overlap of temperature profiles of neighbouring hotspots. The slightly higher temperature on the bottom side at the highest fields can be due to the strong hotspot at  $140^\circ$ , sensor 8.

Figure 7 shows the values of the fit parameters  $P_0$  and  $\gamma$  as a function of  $b = (B_p/B_c)^2$ , where  $B_c = 190$  mT is the critical field at 2 K. Considering  $P_0 = 1/2 R_{s,d} A_d H_p^2$ , where  $R_{s,d}$  and  $A_d$  are the surface resistance and the surface area of the defect, respectively,  $H_p = B_p/\mu_0$ , we obtain  $R_{s,d} A_d \cong 8 \mu\Omega \text{ mm}^2$  from the slope of  $P_0(b)$ . The onset field from the  $x$ -axis intercept of  $P_0(b)$  is 148 mT. If the surface resistance

<sup>1</sup> A factor  $1/d^2$  was missing in Eqs. (38) and (47) of Ref. [6].

Content from this work may be used under the terms of the CC BY 3.0 licence (© 2019). Any distribution of this work must maintain attribution to the author(s), title of the work, publisher, and DOI.

of the defect is that of normal conducting niobium at 10 K,  $\sim 1.5 \text{ m}\Omega$ , the defect area would be  $\sim 5 \times 10^3 \text{ }\mu\text{m}^2$ . The peak temperature rise at the inner surface calculated from Eq. (47) of Ref. [6], for a defect of this size would be  $\sim 2 \text{ K}$ .

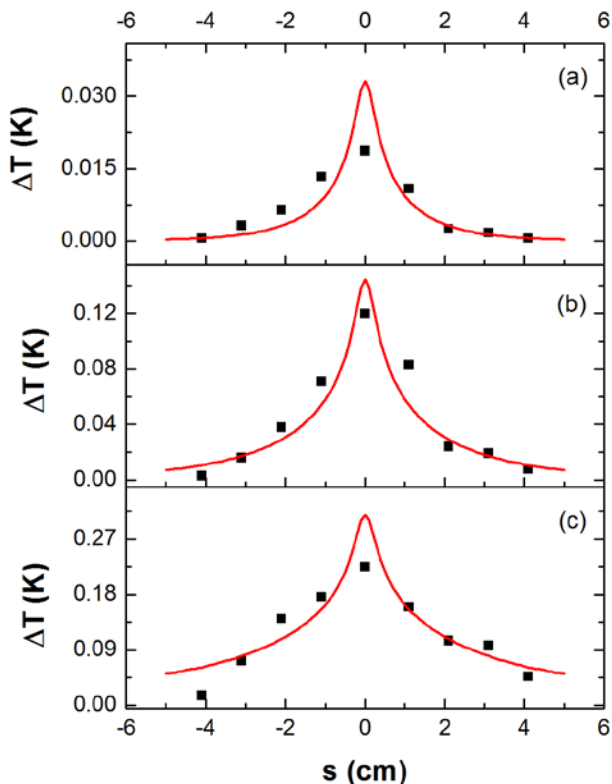


Figure 6: Temperature rise measured on the outer surface of cavity RDT-TD01 at  $130^\circ$  along the meridian, from top (negative  $s$ -values) to bottom, centered at the location of sensor 7 at different  $B_p$ -values: 152 mT (a), 160 mT (b) and 165 mT (c). Solid lines are least-squares fit with Eq. (38) of Ref. [6].

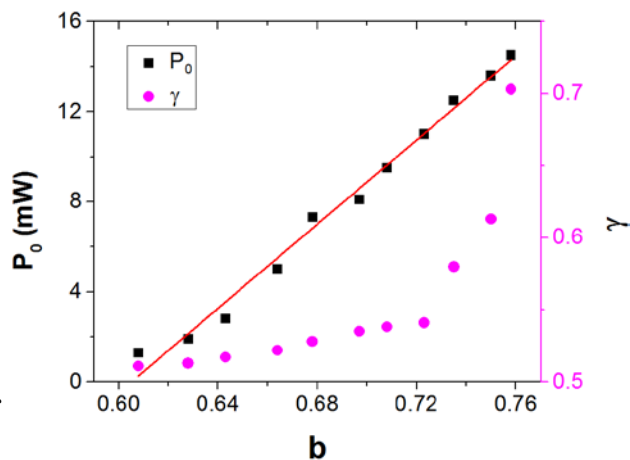


Figure 7: Fit parameters  $P_0$  and  $\gamma$  as a function of  $b = (B_p/B_c)^2$ . The solid line is a linear fit of  $P_0(b)$ .

## DISCUSSION

The results shown in Fig. 2 provide an insight into the maximum dissipated power that a 1.3 GHz Nb cavity at 2.0 K can withstand before reaching thermal instability. The temperature map in Fig. 5 shows that most of the heating is localized between sensors No. 5 and 11, where the magnetic field is within 1% of the peak value. This region corresponds to an area of  $\sim 390 \text{ cm}^2$  and a maximum power density of  $\sim 0.5 \text{ W/cm}^2$  was achieved on average over this area, with an average temperature rise,  $\Delta T \sim 84 \text{ mK}$ . However, the power dissipation is highly non-uniform and  $\Delta T \sim 300 \text{ mK}$  was measured at the hottest spot, corresponding to a local power density of  $\sim 1.8 \text{ W/cm}^2$ . Such power density and the corresponding measured temperature rise indicate that the liquid He is most likely in the film-boiling regime around hot-spots overheated above the critical superfluid temperature.

The power density achieved in cavities EZ-SC-001, RDT-TD01, PJ1-1 and N3 is strikingly different from that of cavities TE1G001 and TE1NS001 since the latter quenched at much lower power dissipation. Similar situation was obtained in cavity TD5, reported in Ref. [7], where the temperature map showed  $\Delta T < 10 \text{ mK}$  at the last point of stability which occurred at  $B_p = 116 \text{ mT}$ ,  $P_{\text{loss}} \sim 6 \text{ W}$  at 2 K. Quench occurring at very low power dissipation also characterizes the performance of Nb cavities treated by nitrogen doping. As an example, N-doped cavity TD#4 in Ref. [8] quenched at  $B_p = 88 \text{ mT}$ ,  $P_{\text{loss}} \sim 1 \text{ W}$  at 2 K and the temperature map showed  $\Delta T < 5 \text{ mK}$ . Given the thermal stability demonstrated in four of the cavities reported in this study, it does not seem plausible that the quenches occurring at low power dissipation and minimal overheating can be caused by heating of normal-conducting defects. It is however plausible that those quenches might be due to an avalanche of vortices entering the surface at a reduced local critical field. Such hypothesis is supported by a hysteretic  $\Delta T(B_p)$  at the quench location, as reported for example in Refs. [6, 8].

Another mechanism of how the high RF power associated with HFSQ could be sustained at fields below the cavity breakdown field  $H_b$ , may be due to the size and spatial distributions of the local power sources revealed by temperature maps. As was shown in Ref. [9] a large areal density of small power sources can result in strong HFQS while only weakly reducing the global field of thermal quench. On the other hand, a few strong local power sources in the cavity equatorial region can ignite lateral thermal quench propagation at  $H > H_b$  without causing much of the HFQS at  $H < H_b$ .

Regarding the hydride model of the HFQS, the availability of four fit parameters in Eq. (1) assures a good fit to the  $R_s(B_p)$  data. However, the values of  $H_0$  shown in Table 2 do not appear plausible, as they are greater than the superheating field of Nb. Given the fit parameters values in Table 2,  $R_s(B_p)$  would saturate at fields above the critical field of Nb, which cannot be reached experimentally. Besides the experimental evidence shown in Fig. 4, it does not seem plausible to expect that  $R_s$  would saturate in the

HFQS region, given that the BCS surface resistance of the areas surrounding the normal-conducting hydrides provides a strong positive thermal feedback.

## CONCLUSIONS

The experimental data of  $Q_0(B_p)$  from four 1.3 GHz SRF Nb cavities showed that some of the cavities exhibit a remarkable thermal stability, sustaining up to ~200 W of power without quench at 2 K. The quality factors for these cavities decrease monotonically with the increasing RF field. Whereas hydrides nano-precipitates could be a source of the hotspots measured in the HFQS, the model proposed in Ref. [2] to describe their effect on  $R_s(B_p)$  cannot explain our data.

Spatial temperature profiles surrounding a hotspot were measured on the outer surface at different fields and were used to gain information on the source at the inner surface, which has a product of surface resistance times the defect area of ~8  $\mu\Omega$  mm<sup>2</sup>. The fact that some cavities can sustain high RF power associated with HFQS may indicate the existence of many weak local power sources which can be due to non-superconducting nano-precipitates or trapped vortex bundles.

## ACKNOWLEDGEMENTS

We would like to acknowledge P. Dhakal, R. Geng, G. Ereemeev and A. Palczewski for providing some of the cavities used for this study and the SRF Cavity Production Group at Jefferson Lab for helping with some of the cavity preparation and cool-down.

## REFERENCES

[1] H. Padamsee, "High-Field Q-slope and Quench Field", in *RF Superconductivity: Science, Technology, and Applications*,

- Weinheim, Germany: WILEY-VCH Verlag, 2009, pp. 129-202.
- [2] A. Romanenko, F. Barkov, L. D. Cooley, and A. Grassellino, "Proximity breakdown of hydrides in superconducting niobium cavities", *Supercon. Sci. Technol.*, vol. 26, p. 035003, Jan. 2013. doi:10.1088/0953-2048/26/3/035003
- [3] B. Aune *et al.*, "Superconducting TESLA cavities", *Phys. Rev. ST Accel. Beams*, vol. 3, p. 092001, Sept. 2000. doi:10.1103/PhysRevSTAB.3.092001
- [4] G. Ciovati and L. Turlington, "A simple variable coupler for the cryogenic test of SRF cavities", presented at the 19th Int. Conf. on RF Superconductivity (SRF'19), Dresden, Germany, July 2019, paper MOP084, this conference.
- [5] G. Ciovati, "Investigation of the superconducting properties of niobium radio-frequency cavities", Ph.D. thesis, Phys. Dept., Old Dominion University, Norfolk, VA, USA, 2005.
- [6] A. Gurevich and G. Ciovati, "Effect of vortex hotspots on the radio-frequency surface resistance of superconductors", *Phys. Rev. B*, vol. 87, p. 054502, Feb. 2013. doi:10.1103/PhysRevB.87.054502
- [7] P. Dhakal, G. Ciovati, and G. R. Myneni, "Role of thermal resistance on the performance of superconducting radio frequency cavities", *Phys. Rev. Accel. Beams*, vol. 20, p. 032003, Mar. 2017. doi:10.1103/PhysRevAccelBeams.20.032003
- [8] J. Makita, G. Ciovati, and P. Dhakal, "Temperature Mapping of Nitrogen-doped Niobium Superconducting Radio-frequency Cavities", in *Proc. 6th Int. Particle Accelerator Conf. (IPAC'15)*, Richmond, VA, Canada, May 2015, pp. 3575-3577. doi:10.18429/JACoW-IPAC2015-WEPWI038
- [9] A. Gurevich, "Multiscale mechanisms of SRF breakdown", *Physica C*, vol. 441, pp. 38-43, July 2006. doi:10.1016/j.physc.2006.03.024.